The Chameleon on the branches: spectral state transition and dips in NGC 247 ULX-1

A. D'Aì [1]*, C. Pinto,[1] M. Del Santo [1], F. Pintore [1], R. Soria,[2,3] A. Robba,[1,4] E. Ambrosi,[1] W. Alston [5], D. Barret,[6] A. C. Fabian [7], F. Fürst,[8] E. Kara [9], P. Kosec,[9] M. Middleton,[10] T. Roberts,[11] G. Rodriguez-Castillo [1] and D. J. Walton [7]

[1]*INAF/IASF Palermo, via Ugo La Malfa 153, I-90146 Palermo, Italy*
[2]*College of Astronomy and Space Sciences, University of the Chinese Academy of Sciences, Beijing 100049, China*
[3]*Sydney Institute for Astronomy, School of Physics A28, The University of Sydney, Sydney, NSW 2006, Australia*
[4]*Università degli studi di Palermo, Dipartimento di Fisica e Chimica, via Archirafi 36, I-90123 Palermo, Italy*
[5]*European Space Agency (ESA), European Space Astronomy Centre (ESAC), E-28691 Villanueva de la Cañada, Madrid, Spain*
[6]*CNRS, IRAP, Université de Toulouse, 9 Avenue du colonel Roche, BP 44346, F-31028 Toulouse, Cedex 4, France*
[7]*Institute of Astronomy, Madingley Road, CB3 0HA Cambridge, UK*
[8]*Quasar Science Resources for ESA, European Space Astronomy Centre (ESAC), E-28691 Villanueva de la Cañada, Madrid, Spain*
[9]*MIT Kavli Institute for Astrophysics and Space Research, Cambridge, MA 02139, USA*
[10]*School of Physics and Astronomy, University of Southampton, Southampton SO17 1BJ, UK*
[11]*Centre for Extragalactic Astronomy and Department of Physics, Durham University, South Road, Durham DH1 3LE, UK*

ABSTRACT

Soft Ultra-Luminous X-ray (ULXs) sources are a subclass of the ULXs that can switch from a supersoft spectral state, where most of the luminosity is emitted below 1 keV, to a soft spectral state with significant emission above 1 keV. In a few systems, dips have been observed. The mechanism behind this state transition and the dips nature are still debated. To investigate these issues, we obtained a long *XMM–Newton* monitoring campaign of a member of this class, NGC 247 ULX-1. We computed the hardness–intensity diagram for the whole data set and identified two different branches: the normal branch and the dipping branch, which we study with four and three hardness–intensity resolved spectra, respectively. All seven spectra are well described by two thermal components: a colder ($kT_{bb} \sim 0.1$–0.2 keV) blackbody, interpreted as emission from the photosphere of a radiatively driven wind, and a hotter ($kT_{disc} \sim 0.6$ keV) multicolour disc blackbody, likely due to reprocessing of radiation emitted from the innermost regions. In addition, a complex pattern of emission and absorption lines has been taken into account based on previous high-resolution spectroscopic results. We studied the evolution of spectral parameters and flux of the two thermal components along the two branches and discuss two scenarios possibly connecting the state transition and the dipping phenomenon. One is based on geometrical occultation of the emitting regions, the other invokes the onset of a propeller effect.

Key words: X-rays: binaries – X-rays: individual: NGC 247 ULX-1.

1 INTRODUCTION

Ultraluminous X-ray sources (ULXs; see Kaaret, Feng & Roberts 2017 and references therein) are point-like, off-nuclear, X-ray sources with isotropic X-ray luminosity above 10^{39} erg s^{-1}, which is the Eddington limit for a $10\,M_\odot$ black hole (BH). Nowadays, it is widely accepted that they are mainly stellar mass compact objects, such as neutron stars (NS) or BHs, accreting matter from a donor above the Eddington limit. Recent discoveries in this field are refining our understanding: coherent pulsations show that NSs are able to accrete at super-Eddington ratios; relativistic winds provided a spectroscopic tool to measure the mass-outflow rate and its effects on to the accretion process; comparative studies on the shape of the broad-band continuum in different sources hint to system inclination

as an important ingredient; the presence of massive companion stars explain the evolutionary path of these systems towards the well-known classical high-mass systems (see e.g. Bachetti et al. 2014; Pinto, Middleton & Fabian 2016; Kosec et al. 2018; Walton et al. 2018).

The X-ray spectra of ULXs can be approximated as power law with indices in a wide range from 1 to 3 in the soft (1–5 keV) band and a cut-off at energies above 10 keV (Bachetti et al. 2014; Pinto et al. 2016; Walton et al. 2018). Of particular interest are the so-called soft ultraluminous sources (SUL) with spectral indices steeper than $\Gamma = 2$ where the bulk of observed emission is likely associated with re-processing of harder X-rays from the central engine by radiatively driven optically thick outflows expected to be present for sources accreting at luminosities exceeding the Eddington limit (Middleton et al. 2015). This gives an opportunity to test extreme accretion regimes rarely observed in other accreting objects such as Galactic X-ray binaries and active galactic nuclei.

*E-mail: antonino.dai@inaf.it

Supersoft ultraluminous X-ray sources (SSUL; also known as ULS in the literature) can be considered a subclass of SUL, showing bolometric luminosities L_{bol} close to, or in excess of 10^{40} erg s^{-1}, but their spectra are completely dominated by blackbody emission at a temperature of ≈ 50–140 eV and associated blackbody radii of ≈ 5–10×10^4 km, with little emission above 1 keV (Urquhart & Soria 2016). They were initially interpreted as a completely different physical class of sources. It was even suggested that the thermal spectrum could be represented by a multicolour emission from a standard Shakura–Sunyaev disc (Shakura & Sunyaev 1973) in the sub-Eddington high/soft state of an accreting BH. In that scenario, the low peak temperature and large radius would be consistent with long-sought-for intermediate mass BHs (e.g. for NGC 247 ULX-1, Tao et al. 2012 estimated $M_{BH} \sim 600\,M_\odot$).

However, from the spectral analysis of a homogeneous sample of SSUL sources, Soria & Kong (2016) and Urquhart & Soria (2016) showed that the temperature–luminosity dependence did not follow the typical $L \propto T^4$ law, expected for sub-Eddington accretion on to a standard Shakura–Sunayev disc, nor the $L \propto T^2$ trend expected for a near-Eddington slim-disc. Instead, they showed an approximate $R \propto T^{-2}$ trend, both for individual sources and across the sample, which argues in favour of emission from an extended, optically thick, photosphere just outside the spherization radius (R_{sph}), where radiation pressure launches the densest outflows (Poutanen et al. 2007). In this scenario, SSULs are considered as ULXs in which the hard photons have been completely reprocessed and thermalized (or, at least, are completely masked from our view). The radial location (size) of the thermal photosphere depends on the physics of the thick inflow/outflow, as well as on the polar angle (Takeuchi, Ohsuga & Mineshige 2013; Middleton et al. 2015).

To test this SSUL/ULX unification scenario, we planned to identify and study in more detail a source that spends some time in the SSUL state and some time at the soft end of the standard ULX classification. This would give us a chance to monitor, for example, how the transition is associated with changes in the blackbody temperature, luminosity, time-variability properties. Such a source exists, in the galaxy NGC 247, as we describe below.

1.1 NGC 247 ULX-1

NGC 247 is a barred, late-type, spiral galaxy at a distance of 3.38 ± 0.06 Mpc (estimated with the Cepheids method; Gieren et al. 2009). It is viewed almost face-on and contains a significant population of X-ray point sources, most likely accreting XRBs, whose brightest member is NGC 247 ULX-1 (Jin et al. 2011). Although the overall star-forming rate in NGC 247 is low ($\approx 0.1\,M_\odot$ yr^{-1}; Davidge 2006), NGC 247 ULX-1 is located (or at least projected) close to an OB stellar association with an estimated age of ≈ 5–40 Myr (Tao et al. 2012). The spectrum of the bright optical counterpart of NGC 247 ULX-1 is compatible with a yellow/blue supergiant with a temperature of $(19\,000 \pm 400)$ K and radius of about $60\,R_\odot$ (Feng et al. 2016). However, a strong caveat is that for most ULX counterparts, it is difficult or impossible to distinguish between the optical emission from the companion star and that from the irradiated accretion disc (Grisé et al. 2012; Ambrosi & Zampieri 2018).

Jin et al. (2011) reported the first detailed X-ray spectral study of NGC 247 ULX-1 from an *XMM–Newton* observation performed in 2009. The spectrum could be satisfactorily modelled by a combination of a soft disc blackbody (or a simple blackbody) of temperature 0.11–0.12 keV, accounting for about 90 per cent of the total emission, and a power-law component, whose photon index could not be tightly constrained, that accounted for the harder part of X-ray spectrum. A possible absorption feature around 1 keV was also detected. In a new *XMM–Newton* observation in 2014 Feng et al. (2016) found the source in a different spectral state, where the flux of the power-law component became comparable to the softer component and NGC 247 ULX-1 appeared for the first time as a standard ULX in the SUL regime. Superposed on this continuum, spectral residuals are sometimes observed around 1 keV; they have been interpreted either as absorption lines from an optically thick, photoionized wind (Jin et al. 2011; Middleton et al. 2014), or/and as emission lines from a hot ($kT \sim 1$ keV) collisionally ionized plasma (Feng et al. 2016). The lack of sufficient energy resolution and the low statistics of those observations have prevented so far an unambiguous determination of the nature of those features, although their presence is generally considered a characteristic property of the SSUL class (see Urquhart & Soria 2016).

In the 2009 observation, Feng et al. (2016) found also X-ray dips in NGC 247 ULX-1 light curve, which seem to be linked to the SUL state occurrence. No increase in the neutral absorption column as a dip occurred was noted, while the continuum appeared generally to soften.

1.2 The recent results from the campaign

With the goal to investigate the nature of the variability, from minutes to hours, in supersoft ULXs, we proposed and were awarded a deep *XMM–Newton* programme on to NGC 247 ULX-1 (PI C. Pinto). The main objective is to know whether such variations in ULXs, and particularly in SSUL, are due to stochastic variability in the wind (at a given mass accretion rate $\dot{M}$) or the clumpy nature of the wind, or a change in the underlying $\dot{M}$.

Observations were carried out between 2019 December 3 and 2020 January 12, collecting approximately 800 ks. Given the rich amount of new information derivable from this campaign, the study of these data has been organized into a series of works that focus on different aspects of NGC 247 ULX-1. Two other papers have recently appeared. The first one, Pinto et al. (2021, hereafter Paper I), searched for evidence of winds mainly thanks to the high-resolution Reflection Grating Spectrometer (RGS) spectra. Two main highly ionized wind components (one in emission and one in absorption) have been discovered. By applying self-consistent plasma models, the absorbing wind component showed a (model-independent) blueshift of $\sim 0.17c$, whereas the emission line pattern has a velocity along our line of sight of $+0.042c$ or $-0.022c$ depending on the use of collisionally- or photoionized plasma models. The second paper, Alston et al. (2021, hereafter Paper II), focused on the temporal variability and on the occurrence and origin of the dipping behaviour. Some preferential time-scales corresponding to quasi-periodic oscillations (QPOs) at frequencies of 4, 9, and 20×10^{-5} Hz were detected in the power spectrum of observations with dips.

The present paper focuses on the X-ray spectral continuum. In particular, we aim to characterize the broad-band spectral variability as a function of the observed accretion state and spectral hardness, constrain the average spectral shape of the source during dip episodes, and understand the occurrence and the spectral changes associated with state transition and the link between the occurrence of dips and the source spectral state. For this work, we used data from the European Photon Imaging Camera (EPIC) detectors: the two Metal Oxide Semiconductor (MOS) cameras and the EPIC-pn, (PN, hereafter) camera. We refer to Paper I for more details on the whole *XMM–Newton* campaign.

2 OBSERVATIONS AND DATA REDUCTION

The NGC 247 campaign comprises eight *XMM–Newton* orbits, with Observation Identifications (ObsID) numbers: 0844860-101/201/301/401/501/601/701/801 (we shall refer to a specific ObsID using these last three digits). All *XMM–Newton*/EPIC observations were acquired through the medium filter using the full window mode. We used the SCIENCE ANALYSIS SYSTEM (SAS) v. 18.0.0 for the extraction and reduction of the *XMM–Newton* data and HEASOFT v. 6.28 for data processing and spectral fitting. Spectral parameter uncertainties are estimated at the 68 per cent confidence level for a single parameter of interest.

We used the tasks EMPROC and EPPROC from the SAS pipeline to process raw data into clean event files. We adopted standard filtering criteria for product generation (FLAG= = 0 and PATTERN ≤ 4 and ≤ 12 for PN and MOS, respectively). We extracted source light curves and spectra using a circular region around the best-known position of NGC 247 ULX-1 (source coordinates taken from Tao et al. 2012) wih a radius of 32 arcsec. We selected a similar circular region for the background region from a source close-by area of the same CCD, but away from its read-out direction, approximately at a distance of 1.5 arcmin from the source coordinates, where no other point-like source was present. The background regions were chosen for each ObsID, after visual inspection of each EPIC image, to ensure the correct application of the abovementioned criteria. Similarly, we produced for each ObsID an energy-selected ($E > 10$ keV) light curve from the source region to remove episodes of high soft protons background according to the standard procedure.[1] This gave us ∼ 620 ks of clean data (per EPIC camera). We corrected light curves for effective area, dead-time and calibration issues using the EPICLCCORR task.

3 LIGHT CURVES, HARDNESS-INTENSITY DIAGRAM, AND SPECTRAL FILTERING

We extracted PN light curves in the 0.2–10 keV energy band using a time bin size of 100 s and estimated their variability in terms of root mean square (RMS) per observation. Data-sets 301, 701, and 801 show low variability (RMS values <10 per cent), whereas ObsIDs 201, 401, 501, and 601 show RMS values >30 per cent due to the presence of dips that last from a few hundreds of seconds to several ks.

To investigate in detail the spectral changes associated with the flux and hardness variations, we performed a hardness–intensity diagram (HID) resolved spectral analysis. To define the soft and hard energy bands, we took the median photon energy of the full time-averaged spectrum, approximately 0.9 keV, the energy at which there is also the strongest spectral curvature (see e.g. Paper I). We extracted energy-selected, background-subtracted, corrected light curves in the 0.2–0.9 keV and 0.9–10.0 keV energy bands with 100 s bin size and computed the hardness ratio (HR; defined as the hard-to-soft count rate ratio). However, due to the low statistics, the HR suffers from a high Poisson noise. To mitigate this noisy HR, we fitted each ObsID light curve with an interpolating smoothing function.[2] We then computed the HR curve based on the hard and soft interpolating

function values. In Fig. 1, we show the resulting HID as a 2D density histogram, where colours indicate the point density, and, consequently, the exposure time.

The total HID shows two distinct branches, which We shall refer to as the normal and dipping branches. To study the spectral changes occurring in the different zones of the HID, but still working with high signal-to-noise ratio (SNR) spectra, we selected a total of seven regions on to the HID from which we extracted the relative good-time intervals (GTIs). The limits of the boundary regions were chosen to ensure enough statistics per spectrum as follows: HR <0.45, 0.45 ≤ HR <0.70, HR ≥ 0.70. Then, since in the normal branch the HR extends up to about 1.3 and the statistics is higher, we divided the third region of this branch in two parts at HR = 0.95. These regions are shown in Fig. 1. Observations with high variability and presence of many dips tend to populate the dipping branch, and, preferentially, the upper part of the normal branch as shown for ObsIDs 401, 501, and 601 (see Fig. 2, where the light curve points are coloured according to the colour scheme of the regions of Fig. 1). Observations characterized by low variability occupy a compact region of the HID in the bottom part of the normal branch (see e.g. ObsID 301, 701, and 801, Fig. 2). ObsID 201 is in-between the two classes, as its points populate both the dipping branch and the lower part of the normal branch, due to the presence of just one, moderately long, dip at the beginning of the observation, after which the source goes rapidly in the middle and, at the end of the observation, in the bottom of the normal branch. Both branches show a positive correlation between count rate and hardness, thus higher observed rates correspond to harder spectra.

We will label SSUL the supersoft state region at the bottom of the normal branch; from SUL1 to SUL3 the regions of the upper part of the normal branch; from D3 to D1, the regions from the upper to the lower part of the dipping branch. From these HID selections, we derived the GTIs to filter both source and background spectra for all the EPIC instruments in each ObsID. After having verified the full compatibility of the MOS1 and MOS2 spectral products, we produced stacked spectral products (source, background, and response matrices) using the `epicscombine` tool and refer to these combined products as the MOS12 products. PN and MOS12 spectra belonging to the same HID region from any ObsId were finally added using ADDASCASPEC.

We re-binned MOS12 and PN spectra with the SPECGROUP tool, adopting a minimum SNR of three, requiring no more than three energy channels per resolution element, and a minimum number of 25 counts per channel to use the χ^2 statistics. We performed spectral fits in the 0.6–10 keV and 0.3–10 keV bands for PN and MOS12 spectra, respectively. We report the total exposure times and average count rates for the intensity-HID resolved PN and MOS spectra in Table 1.

4 FIT PROCEDURE AND RESULTS

The continuum emission of this source has been modelled in the past using different combinations of soft thermal component and a power law for the hard component (Jin et al. 2011; Feng et al. 2016). The continuum time-averaged spectrum of all these observations has been modelled by Paper I with a combination of three blackbodies. For our HID-selected spectra, we found that the combination of a soft blackbody and a multicolour disc blackbody component (`diskbb` in XSPEC) resulted in satisfactorily fits without the need of an additional third component (see Pintore et al. 2015, for a similar approach for the similar source NGC 55 ULX-1). We caution the reader that referring to this disc component flux and temperature in what follows, we do

---

[1]https://www.cosmos.esa.int/web/xmm-newton/sas-thread-epic-filterbackground

[2]We adopted the Savitzky-Golay filter present in the *SciPy* module (https://docs.scipy.org/doc/scipy/reference/generated/scipy.signal.savgol_filter.html) with 15–21 typical windows depending on the variability associated to each ObsID
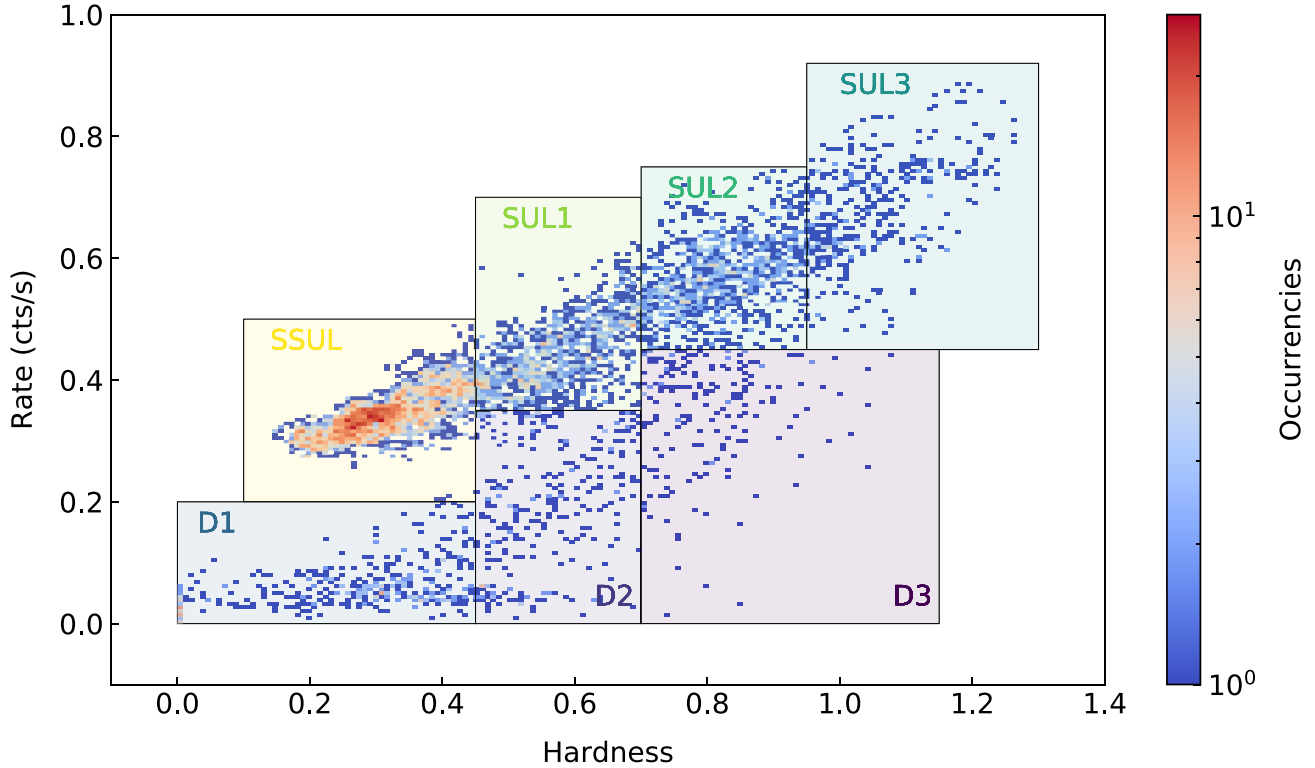
Figure 1. 2D density plot of the hardness–intensity diagram from the whole set of *XMM–Newton* observations examined in this work. Right bar show the colour gradient in log scale. Boxes and labels show the regions used for the spectral products extraction.

not interpret it physically associated with emission from a standard sub-Eddington disc. The spectral disc shape serves to fit all the internal hard X-ray reprocessed emission, whose primary shape is not accessible to us.

This continuum is absorbed by an equivalent hydrogen column density N_H modelled with the tbabs component, with element abundances from Wilms, Allen & McCray (2000) and atom cross-sections from Verner et al. (1996). For all fits the N_H parameter was fixed to the best-fitting value of the time-averaged (over all the observations) spectrum (1.7×10^{21} cm^{-2}) as we noted this parameter did not significantly vary for the different spectra.

The correct modelling of the emission/absorption features is not trivial. To limit the model parameter degeneracy due to the low energy resolution of the EPIC in the soft band, the apparent broadening of the line profiles, the shifts in the line positions in correlation with the flux state, we took advantage of the time-averaged high-resolution RGS analysis reported in Paper I. From the Gaussian line scan, we retrieved the energy of the most significant emission/absorption lines. We interpret these lines as generated by two different plasma environments. For the emission line pattern, we fixed the normalizations and the centroids of all the lines to the RGS best-fitting results (see Table 2) and left in the fit procedure a common multiplicative flux constant (C_{em}) free to vary for the whole set of lines. This thin plasma is parametrized as a comoving single region where lines share a common width (σ_{em}). Our set of fitted lines does not comprehend all the possible transitions involved in a physical plasma model as shown in Paper I. Although in the RGS all the lines are resolved with a few eV width, the EPIC spectra strongly requires a width larger than the spectral resolution of the PN and MOS CCDs (~ 100 and 60 eV, full-width half-maximum at 1 keV, respectively). In our choice this broadening accounts for the vaster

pattern of close-by blended lines and a possible state-dependent physical broadening. As a necessary further check, we also refitted our spectra by leaving the line widths of the single detected lines free to vary in a closed neighbourhood (around 0.1 keV) of our best-fitting parameters, and we did not note any statistically significant difference from the common best-fitting values.

We observed significant shifts in the line energies for the different HID-resolved spectra (similarly to what is already shown in the spectra averaged over the single ObsIDs, see Paper I). To consistently evaluate these shifts we assume that the relative line pattern remains unchanged for the different spectra and let a common shift parameter free to vary. For this fitting purpose, we modelled the lines using the zgauss component, and the redshift parameter z_{em} is free to vary. This choice proved a posteriori a satisfactorily way to flatten the residuals at the different line energies without the risk of increasing the parameters degeneracy.

The same fitting procedure is adopted for the complex of the absorption lines; in particular, we introduced in analogy with the emission line pattern a similar set of parameters: C_{abs}, σ_{abs}, and z_{abs} for the relative multiplicative absorption normalization constant, common absorption line width, and relative absorption line redshift, respectively. In the fitting process, if we obtained only an upper limit to the C_{abs} value (the 90 per cent c.l. value is reported in Table 3), we set this parameter to 0 (freezing also the σ_{abs} and z_{abs} parameters) for the computation of best-fitting values and uncertainties of all other parameters. Finally, a normalization constant between the PN and the MOS12 spectra is left free to vary to account for any residual flux intercalibration mismatch. The constant is frozen to 1 for the PN spectrum, and free to vary for the MOS12 model (C_{mos12} parameter). Our model in xspec reads as: $C_{mos12} \times$ tbabs $\times$ (bbody+diskbb + $C_{em} \times$ (zgau$_1$ + zgau$_2$
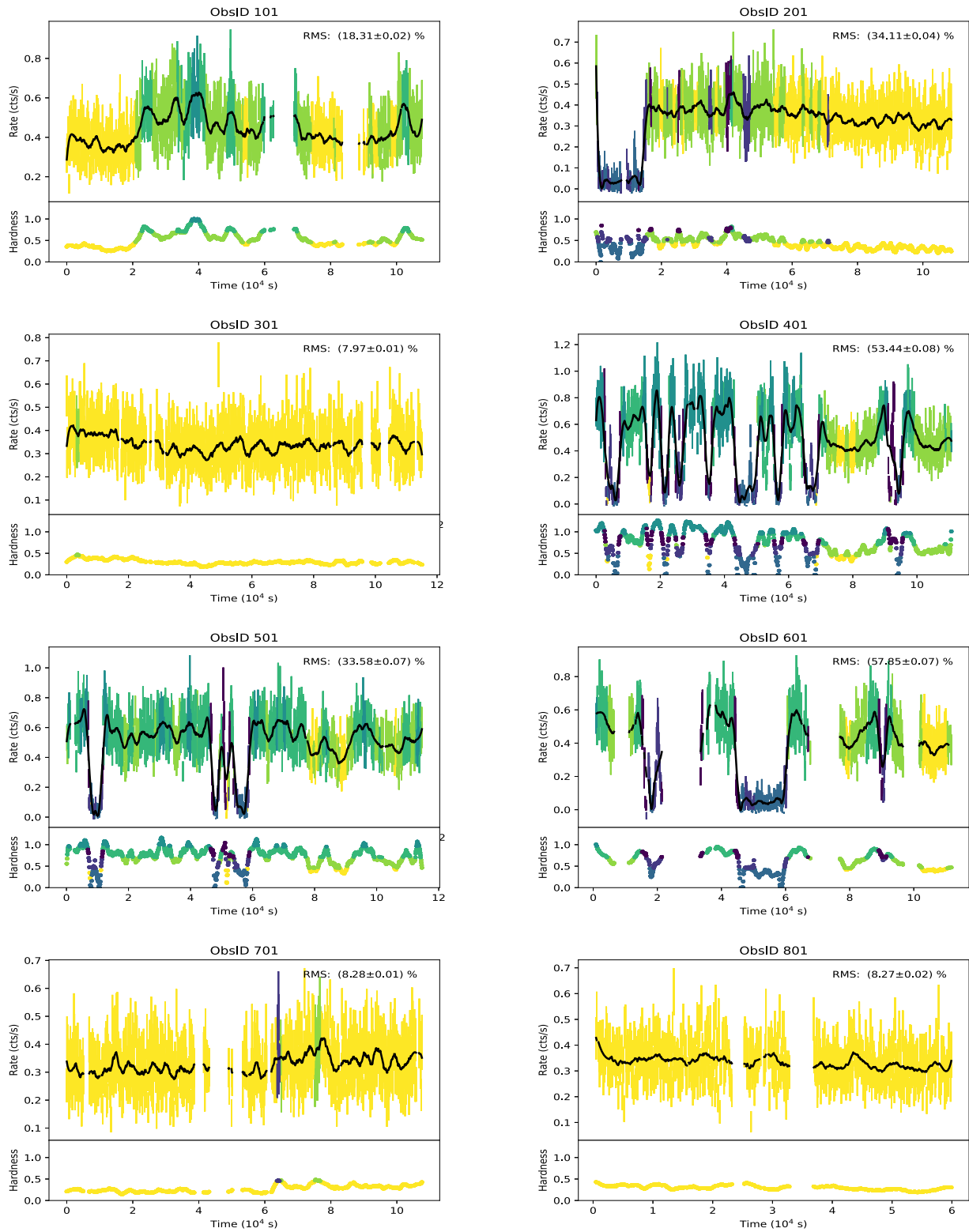
Figure 2. EPIC/PN light curves of each ObsID (time bin-size 100s). Overplotted the best-fitting smoothing curve (continuous black line). Lower panels show the corresponding hardness (0.9–10 keV / 0.2–0.0.9 keV) curve. Colours identify the good-time intervals used for spectral extraction according to the colour scheme shown in Fig. 1.

Table 1. Total exposures and background-subtracted average count rates (0.6–10 keV and 0.3–10.0 keV energy bands for PN and MOS12, respectively) for the PN and MOS12 HID-selected spectra.

		Exposure times 10^4 s		Count rates 10^{-2} counts s^{-1}	
	State	PN	MOS12	PN	MOS12
Normal branch	SSUL	29.3	33.9	19.7	10.0
	SUL1	14.4	16.3	27.6	15.2
	SUL2	7.9	9.0	39.3	21.8
	SUL3	3.4	4.1	47.1	26.3
Dipping branch	D3	1.0	1.2	20.8	12.5
	D2	2.4	2.7	8.6	4.4
	D1	3.8	4.3	3.2	1.7

Table 2. Emission and absorption line patterns as estimated from the EPIC-RGS time-averaged spectrum (see Paper I). Energy positions (E_{fix}) and line normalizations (N_{fix}) are frozen in the fits. Absorption/emission lines have tied line widths (σ_{em} and σ_{abs}) and a common multiplicative constant factor (C_{abs} and C_{abs}), left free to vary in the fits (parameters reported in Table 3).

	E_{fix} keV	E_{rest} (Id.) keV	N_{fix} 10^{-6} ph cm^{-1} s^{-1}
		Emission lines	
zgau$_1$	0.5920	O VII-VIII	5.8
zgau$_2$	0.8865	Ne IX-Fe XVIII	8.5
zgau$_3$	0.9766	Ne X-Fe XX-XXI	6.6
zgau$_4$	1.5540	Mg XI-XII	0.33
		Absorption lines	
zgau$_5$	0.7483	O VIII	−0.544
zgau$_6$	1.1813	Ne X-Fe XXI	−2.73
zgau$_7$	1.2845	Fe XXIII-XXIV	−2.34

+ zgau$_3$ + zgau$_4$) + C$_{abs}$ × (zgau$_5$ + zgau$_6$ + zgau$_7$)).

We emphasize that, despite our best efforts the modelling described above is still limited by quality of the available data, i.e. counting statistics and energy resolution of the EPIC cameras. Nevertheless, our results appear consistent with the full time-averaged RGS results (Paper I), so we are confident that they are reasonably robust. Future observations with instruments with higher energy resolution such as *XRISM* (XRISM Science Team 2020) or *ATHENA* (Barret et al. 2020) could be beneficial for firmly constraining this variable emission/absorption line landscape.

In Table 3, we report the final results of the fit for each selected spectrum. As it can be noted the final χ^2 are not always formally acceptable (reduced $\chi^2 \gg 1$), although the data overall appear reasonably well fitted (Fig. 3). The largest contributions to the final χ^2 are due to unaccounted local features in energy bands which are not covered by the RGS spectral analysis (e.g. in the 2–3 keV range) or by unmodelled residuals in the low-energy part of the spectrum (0.5–0.7 keV) in some cases. In order to compare the spectral parameters without biases introduced by statistically poor local features (detection significance $\leq 3\sigma$), we left these residuals unmodelled. In Fig. 3, we show the seven energy spectra and the unfolded unabsorbed best-fitting models.

The SSUL state includes the low variability spectra (e.g. ObsID 301, 701, and 801). Because of the long integrated exposure, the stacked spectrum has a very high SNR. The absorption line pattern is clearly detected at a $\Delta\chi^2 = 140$ (statistical difference with respect to a model where $C_{abs} = 0$). The SUL1 spectrum gets a good fraction of the total exposure from ObsID 101, which shows

no dips but a significant higher average count rate. The pattern of absorption lines is still detected, albeit at a lower significance with respect to SSUL, with $\Delta\chi^2 = 22$. SUL2 and SUL3 spectra are populated by the most variable observations (e.g. ObsID 301, 401, and 501). We found no significant evidence for the absorption line pattern in any of these spectra. The overall statistics for the dipping branch spectra is much lower than in the spectra extracted from the normal branch. For this reason, determination of all the parameters is subjected to larger uncertainties, particularly for the temperature and normalization of the DISKBB component. As shown in Table 3, the range of disc temperature values for normal branch spectra is 0.5–0.64 keV; at 90 per cent confidence level, we found a lower limit on the kT_{disc} value of 0.53 keV in the D3 spectrum, whereas in D1 and D2 any value of kT_{disc} in this range does not significantly change the χ^2 value of the fit. We therefore freeze the kT_{disc} parameter in D1–D3 spectral fits to the best-fitting value obtained for the SUL3 spectrum ($kT_{disc} = 0.64$ keV) because before any dip episode the most likely position of the source was in the SUL3 region. We note that setting this value to the lower limit ($kT_{disc} = 0.5$ keV) would raise the inner disc radius by a factor of ~ 2, while the fluxes of all the spectral components and the other parameters would remain consistent within the statistical uncertainties reported in Table 3. We found no statistical evidence for the presence of the absorption lines in any of these spectra, though the C_{abs} upper limits do not rule them out.

4.1 Spectral variability along the branches

NGC 247 ULX-1 shows the highest luminosity ($\sim 2.3 \times 10^{39}$ erg s^{-1}) in SUL3, whereas previous studies on this source reported on a maximum luminosity of about 10^{40} erg s^{-1} (Feng et al. 2016). We verified that such discrepancy is entirely due to our lower estimate of the absorption column.

The bolometric luminosity decreases along the normal branch towards the SSUL of a factor of 1.5. This change in the luminosity is mainly driven by the DISKBB component. Indeed, the fractional variation of the BBODY component is only about 10 per cent, whereas the DISKBB luminosity increases by a factor of 6 as shown in the upper panel of Fig. 4. The ratio of the bolometric luminosity (0.01–10 keV) between the blackbody and the disc components in the SSUL state reaches a value ~ 15, while in the SUL1-SUL3 this ratio ranges between 2 and 4 (lower panel of Fig. 4). This is the most significant characteristic that distinguishes the SSUL state from all the other spectral states, as we did not find any evidence for intermediate values.

We show in Fig. 5 the basic parameter relations as a function of the source state for the two continuum components. From SSUL along the normal branch we observe an increasing of the BBODY temperature, from 0.15 to 0.2 keV, and a decreasing of the associated emitting radius. For the disc component, the SSUL→SUL1 passage is mainly due to a geometrical change in the observable part of the system, i.e. more area from the DISKBB component is visible, whereas the source shifts in the more variable part of the upper branch are due to (albeit small) changes in the emitting peak temperature of this component.

The dipping branch is divided in three spectra: the D3 region characterizes mainly the ingress/egress passages, the D2 region the intermediate dip flux and D1 the lowest flux observed in the dip. We observe that the bolometric luminosity rapidly decreases up to a factor of 10 compared to the normal branch, with a luminosity of 3×10^{38} erg s^{-1} in D1 (Table 3). The softening observed along the dipping phase is due to both the decreasing of the black-body

Table 3. Best-fitting results. Unabsorbed luminosity calculated in the 0.01–10 keV range with respect to the *EPIC/PN* spectrum, assuming isotropy and 3.4 Mpc distance. For R_{disc} we assumed a disc inclination of 60°. C_{em} and C_{abs} are multiplicative model normalization constants for the optically thin/thick line emitting/absorbing line patterns. L_{abs} is the difference in luminosity between the best-fitting model and a model with C_{abs} set to zero. Errors are given at 1 σ c.l.

				Continuum				
Spectrum	kT_{bb} eV	R_{bb} 10^3 km	L_{bb} 10^{38} erg s^{-1}	kT_{disc} eV	R_{disc} 10^2 km	L_{disc} 10^{38} erg s^{-1}	L_{tot} 10^{38} erg s^{-1}	C_{mos12}
SSUL	147 ± 3	4.73 ± 0.19	12.9 ± 1.1	510 ± 40	1.0 ± 0.3	0.88 ± 0.09	15.01 ± 0.22	1.032 ± 0.007
SUL1	160 ± 4	3.60 ± 0.13	11.5 ± 0.5	500 ± 20	2.1 ± 0.3	3.3 ± 0.4	16.6 ± 0.3	1.041 ± 0.009
SUL2	188 ± 3	2.96 ± 0.08	13.3 ± 0.5	610 ± 20	1.73 ± 0.17	5.1 ± 0.4	20.3 ± 0.3	1.019 ± 0.010
SUL3	200 ± 4	2.68 ± 0.09	14.3 ± 1.0	640 ± 30	1.9 ± 0.3	7.5 ± 0.7	23.5 ± 0.4	1.002 ± 0.012
D3	173 ± 6	2.63 ± 0.25	7.5 ± 0.9	640‡	1.21 ± 0.05	3.0 ± 0.3	9.7 ± 0.6	1.09 ± 0.04
D2	140 ± 4	3.3 ± 0.3	5.2 ± 0.4	640‡	0.73 ± 0.03	1.1 ± 0.1	6.7 ± 0.5	1.08 ± 0.04
D1	128 ± 5	2.7 ± 0.3	2.4 ± 0.3	640‡	0.37 ± 0.03	0.30 ± 0.05	2.9 ± 0.3	1.05 ± 0.05

				Emission/absorption line pattern					
Spectrum	C_{em}	σ_{em} eV	z_{em} 10^{-2}	L_{em} 10^{38} erg s^{-1}	C_{abs}	σ_{abs} eV	z_{abs} 10^{-2}	L_{abs} 10^{38} erg s^{-1}	χ_ν^2/dof
SSUL	4.8 ± 0.4	87 ± 5	5.6 ± 0.5	1.70 ± 0.08	3.4 ± 0.7	130 ± 17	3.1 ± 1.5	−0.47	150/94
SUL1	4.9 ± 0.6	110 ± 8	1.9 ± 0.7	1.9 ± 0.2	0.75 ± 0.20	35 ± 20	−4.9 ± 1.0	−0.12	155/117
SUL2	4.7 ± 0.6	120 ± 10	−1.6 ± 1.0	1.9 ± 0.2	<0.4†	50‡	0‡	...	141/139
SUL3	4.0 ± 0.8	120 ± 20	−5.7 ± 1.6	1.7 ± 0.3	<1.9†	50‡	0‡	...	169/136
D3	2.8 ± 0.9	100 ± 30	−1.1 ± 2.9	1.2 ± 0.2	<1.4†	50‡	0‡	...	73/78
D2	1.2 ± 0.4	50 ± 30	6.5 ± 1.9	0.43 ± 0.11	<3.0†	50‡	0‡	...	61/58
D1	0.64 ± 0.18	50 ± 30	8.2 ± 2.2	0.21 ± 0.06	<0.14†	50‡	0‡	...	38/41

Notes. † 90 per cent upper limit calculate with $\sigma_{abs} = 50$ eV and $z_{abs} = 0$.   ‡ fixed parameter

temperature (from 0.17 keV in D3 to 0.13 keV in D1) and the stronger attenuation of the disc emission of a factor of 10 from D3 to D1 compared to the blackbody component which is of a factor of 3.

Finally, the emission lines pattern shows significant variability both in energy and width. These parameters appears to be strongly correlated with flux of the disc component. On the other hand, the overall line flux is constant in the normal branch, while it decreases along the dipping. We point out that detailed investigation of the line emission/absorption pattern can only be constrained with the application of self-consistent photo- or collisionally ionized models which requires combined EPIC and high-resolution spectra. However, this is beyond the scope of this study.

5 SEARCH FOR PERIODIC VARIABILITY

We performed a search for periodic signals in all 8 *XMM–Newton* light curves of NGC 247 ULX-1, following the procedure outlined in Israel & Stella (1996). Other than the standard procedure with a single power spectra density (PSD), we took into account period shifts, which may smooth out the signal in the single PSD, since such period variations are observed in most PULXs (Pulsating ULXs; see i.e. Israel et al. 2016). To this end, we corrected the time of arrival (ToA) of the source events, in each observation, for a grid of $\sim 10\,000$ points, by a factor of $-\frac{1}{2}\frac{\dot{P}}{P}t^2$, in the range $7\times10^{-6} < |\frac{\dot{P}}{P}\,(s^{-1})| < 1 \times 10^{-11}$, where $\dot{P}$ is the first period derivative (see Rodríguez Castillo et al. 2020 for details).

No significant coherent signals were detected; we calculated a 3σ upper limit around 8 per cent–11 per cent for the pulsed fraction (PF) of signals in the data, PF here defined as the semiamplitude of the signal sinusoid divided by the average count rate. A marginal detection of a coherent signal at ~ 23 s was detected with PF ~ 5 per cent, but which we were not able to confirm, as it was not present in any other data set after applying the corresponding

corrections to the photons ToA, and the high number of PSD (about 90 000) statistically makes possible, in principle, the occurrence of such a signal by chance.

6 DISCUSSION

In this paper, we focused on the broad-band spectral changes observed in a deep *XMM–Newton* observational campaign of NGC 247 ULX-1. Previous studies in this source already noted a spectral bimodality, where on a typical *XMM–Newton* observing window (around 100 ks), NGC 247 ULX-1 preferentially was found either in the so-called SSUL state, or in a relatively harder, more luminous state where dipping activity is also present (SUL state; Feng et al. 2016). One interesting exception is found in ObsID 02, where we clearly spotted a full transition from a dip, followed by a period in the SUL state, and then to the SSUL on a time-scale of just a few hours. The source spent a 47 per cent, 41 per cent, and 12 per cent of the observing time in the supersoft (SSUL), soft (SUL1-SUL3), and dip states (D1-D3), suggesting that transition from SSUL to SUL can happen once every few days. The fractions of low- and high-flux states is also consistent with previous *Swift* monitoring campaign (see Feng et al. 2016). The SSUL state always occupies a well-defined and compact region in the HID and shows no significant spectral variability on time-scale as long as hundreds of ks. On the contrary, once the SUL state sets in, the source populates a larger HID area, creating a clear diagonal track. As shown in Fig. 1, the SSUL high density compactness might indicate a physical limit of the source or a tight geometric constraint. As dips occur, a lower branch is created beneath the normal one.

The source shows some preferred tracks in its movement along the HID. Dips occur as the source is in the SUL regime, either from SUL2 or from SUL3 regions; ingress and egress times populate the D3 and D2 spectra, whereas the D1 spectrum comes from the time segments characterized by the lowest count rate (deep dip). We noted that
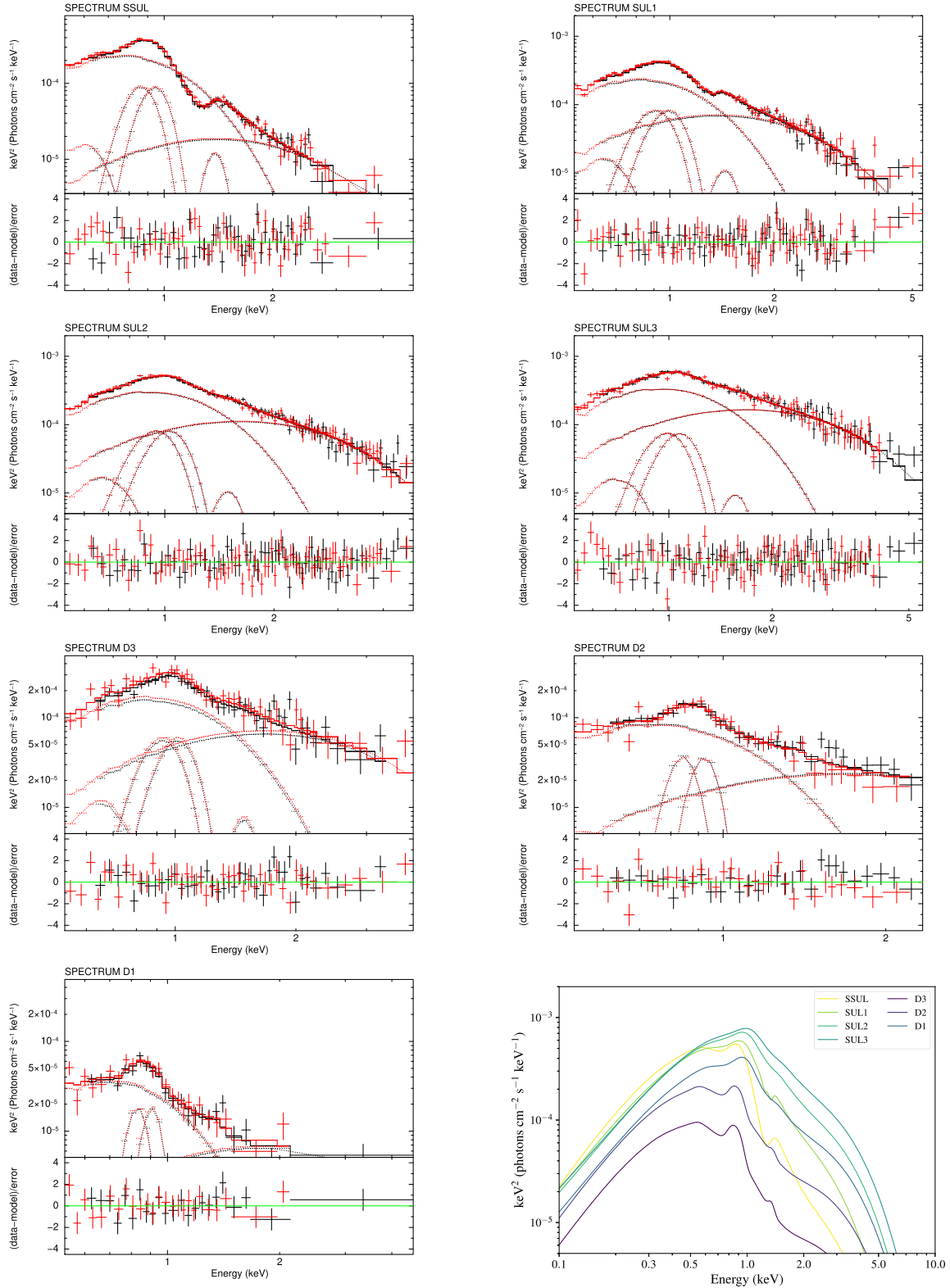
Figure 3. Unfolded energy spectra and residuals in units of σ for the all the HID-selected spectra (black and red data for the EPIC/PN and MOS12 data, respectively). Last figure comprehensively shows all the best-fitting unabsorbed models in the 0.1–10 keV range in the $E^2 \times f(E)$ representation.

during the longest dips, the source occasionally switched to harder flaring episodes in D2 state. Most dips show the following pattern: SUL2/SUL3 → D3 → D2 → D1 → D2 → D3 → SUL2/SUL3. The passage from the SSUL to SUL state is only occasionally

observed. We selected seven regions on the HID and extracted the corresponding spectra. For the normal branch spectra, the continuum emission is well fitted with two thermal components: a soft blackbody and a disc multicolour blackbody. The blackbody emission represents
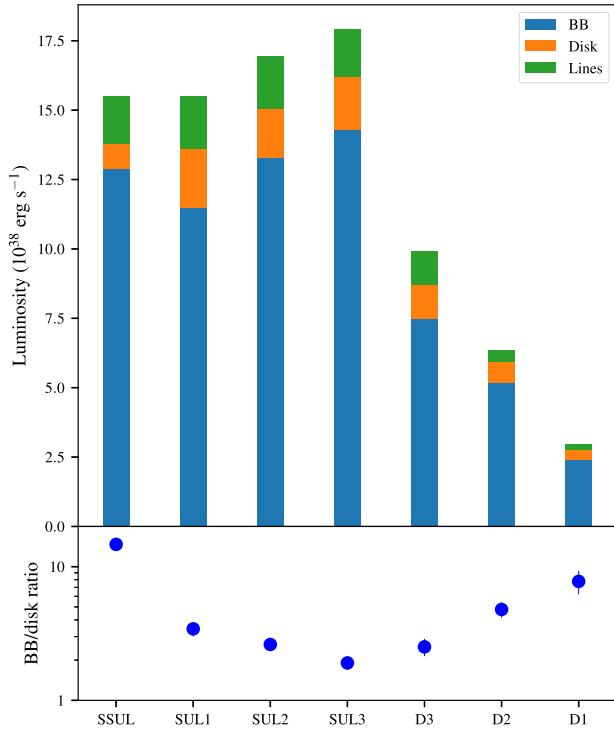
Figure 4. Unabsorbed luminosity (0.01–10 keV range) of the two continuum components as a function of the HID-selected regions.


Figure 5. HID resolved continuum parameters evolution. From top to bottom panel: dependence of the blackbody temperature, blackbody radius, disc blackbody temperature, and disc radius on the HID selected spectrum. Temperatures in units of keV, radii in units of km.

the bulk of the emitted power in each spectrum. It is likely due to strong reprocessing in an optically thick environment formed at R_{sph}, where disc inflow is mainly inflated by internal radiation pressure. This picture is consistent with the observed low temperature, large radius, and super-Eddington luminosity (see Shen et al. 2015; Soria & Kong 2016; Urquhart & Soria 2016; Guo et al. 2019). The hotter component, which we fitted using a DISKBB, dominates the emission above 2 keV. Although its origin is still debated, it might come from internal hard X-ray emission, which has been inefficiently reprocessed, or simply scattered along our line of sight. Alternatively, it can be continuum emission (bremsshtrahlung and/or Comptonization) from an extended optically thin plasma where the emission lines are produced, or a tail of the blackbody emission which has been Compton upscattered in a coronal environment around the photosphere. In addition to the continuum, we added multiple emission and absorption lines derived by the combined averaged PN / RGS analysis to mimic the emitting and absorbing plasmas found in Paper I. Their shifts suggest different Doppler motions in several states as a consequence of a velocity field which changes depending on the launching site and on the geometry of the system. This seems supported by correlations among the parameters of the emission lines and the underneath hard X-ray flux (see Table 3). However, given the limited energy resolution of the EPIC we are not able to distinguish between a varying ionization state of the plasma, the effect of a different line broadening for the different ionized species, a complex absorption/emission pattern. A thorough study of the lines is left to a dedicated forthcoming study. For consistency the same spectral model has been applied also to the dipping branch spectra, although the physical conditions in and out of the dips might be different.
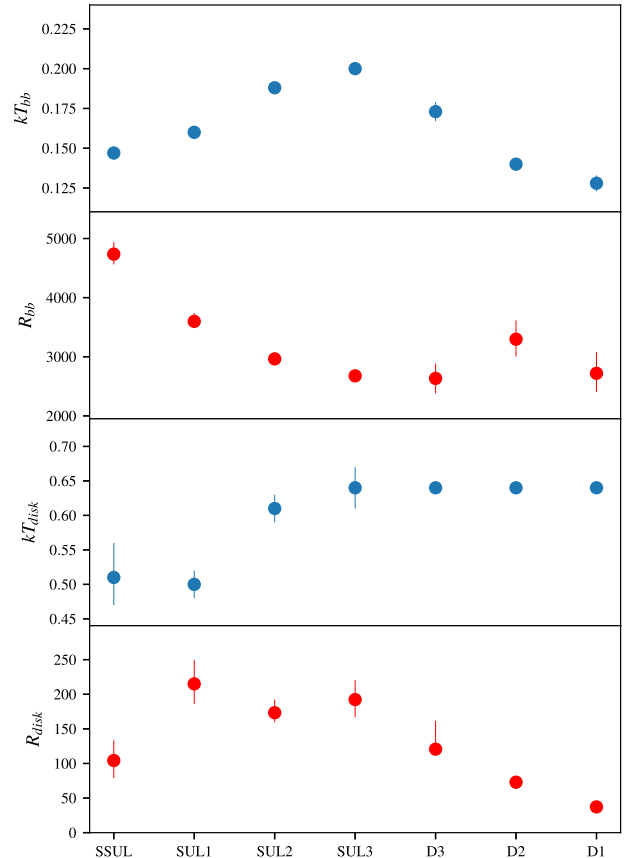
6.1 The normal branch: from SSUL to SUL

In the normal branch, although the luminosity of the BBODY flux component remains almost constant, kT_{bb} and R_{bb} vary clearly in anticorrelation. From SSUL to SUL3 the kT_{bb} increases from 0.14 to 0.2 keV, while R_{bb} decreases from 4.7 to 2.7×10^3 km (see Table 3). At variance with classical Galactic XRBs, where higher temperature and flux of a thermal component are usually explained as an increase in the local accretion rate in SSUL ULXs that may not be the case. The observed emitting region dissipates locally at R_{sph} and, at the same time, reprocesses and re-emits part of the internal hard X-ray radiation. The fraction of the reprocessed power might strongly depend on the subtended angle, on how internal radiation is beamed, and on the disc torus height. According to Poutanen et al. (2007), a super-Eddington disc has a photosphere, where the optical depth is close to unity, at a certain radius R_{ph}, which is proportional to the mass accretion rate $R_{ph} \propto \dot{m}_0^{2/3}$, where $\dot{m}_0 = \dot{M}_0/\dot{M}_{Edd}$ is the dimensionless accretion rate. If the blackbody radii derived from the fits are linked to this physical radius, then we estimate a decrease in the accretion rate by ~ 40 per cent from the SSUL to the SUL3 region (see Table 3). On the other hand, the corresponding blackbody temperature, is anticorrelated with $\dot{m}_0$ as $T_{sph} \propto \dot{m}_0^{-1/2}$. Considering in particular the outflowing photosphere model of Soria & Kong (2016), our results fit well into the vast sample of supersoft ULX sources analysed by Urquhart & Soria (2016), when we restrict to the normal branch results. Extending the validity of this model to the
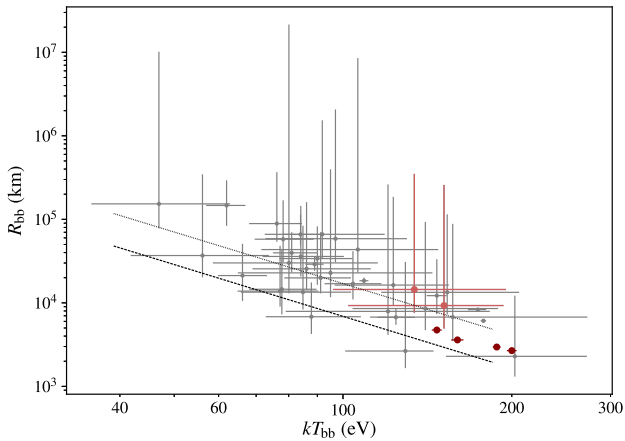
Figure 6. Radius and temperature correlation from a sample of ULS (from Urquhart & Soria 2016). The light red points are from two observations of NGC 247 ULX-1 studied in that paper. Our new measurements for the four spectra of the normal branch are dark red coloured. The dotted and the dashed lines show expected relations for a $10\,M_\odot$ BH and for a $1.4\,M_\odot$ NS according to the calculations of Soria & Kong (2016).

dipping branch spectra could, in fact, be misleading. As it will be discussed in the next section, the mechanism behind the dips is likely not a smooth variation of the accretion rate, but a sudden change either in the observing geometry, which significantly covers part of the emitting regions, or an abrupt change in the overall accretion rate. In both cases, the spectral shape of the softer component depends on additional conditions besides the $\dot{m}_0$ value. Therefore, we inserted only the new points of NGC 247 ULX-1 obtained from our four normal branch spectra to this sample (see Fig. 6). In the same plot, we reproduced the expected kT_{bb} versus R_{bb} relation for a $10\,M_\odot$ BH and for a $1.4\,M_\odot$ NS according to the calculations of Soria & Kong (2016). Our new values appear compatible with the overall trend found by Urquhart & Soria (2016) and suggest in the outflowing scenario of Soria & Kong (2016) either a massive NS (which is likely given the high accretion rate) or a light stellar-mass BH, though this runs contrary to predictions given in Yao & Feng (2019), who estimated a BH mass in the range 15–60 $M_\odot$ based on the fit result of a disc irradiation model (Meier 2012) applied to the UV/optical spectrum of the source.

According to this scenario highest accretion rate would be thus reached in SSUL state, even though the bolometric luminosity increases going towards SUL3. The observed luminosity should scale as the logarithm of the accretion rate, so part of the luminosity in SSUL should be missed. There are many channels where this extraluminosity might indeed hide: stronger emission in the UV regime (as the blackbody temperature decreases, the fraction of the total power emitted out of band correspondingly increases, so it becomes more important to cover also the line and edge structures of the UV band to retrieve its proper measure), or transfer into kinetic power of outflows (we already noted that absorption lines seem stronger in SSUL state), or geometric effects (i.e. a change in the funnelling angle, where the region responsible for the harder emission become out of sight in SSUL state, which might also be linked to its compactness in the HID).

Guo et al. (2019) interpreted the SSUL/SUL transition according to the thick-disc model of Gu et al. (2016), where the key physical parameter is the changing geometrical configuration of the system. This model also predicts the highest accretion rate in the SSUL regime where the inner regions are more obscured. In a possible

alternative scenario, the increasingly brighter hard tail, from SSUL to SUL, could be produced by an increase in the accretion rate which boosts the emission from the inner super-Eddington regions, followed by further scattering through the outer disc/wind (Walton et al. 2020; Gúrpide et al. 2021). This has been invoked to explain the lower pulse fraction at higher X-ray fluxes of some ULXs (Mushtukov et al. 2021; Robba et al. 2021).

6.2 The origin of the dips

Few ULXs show dips, e.g. NGC 55 ULX-1 (Stobbart, Roberts & Warwick 2004) and NGC 5408 ULX-1 (Grisé et al. 2013), that also have in common with NGC 247 ULX-1 a soft spectral peak (< 1 keV) and the presence of local emission features (Sutton, Roberts & Middleton 2015) and strong absorption lines from the wind (Pinto et al. 2016, 2017).

Similarly to what is observed in Galactic accreting binaries, the presence of dips might indicate that we are seeing these systems at high inclination angle. However, in classical Galactic XRBs, dips are caused by transient obscuration of the X-rays from an accretion bulge, or an outer disc structure (White & Swank 1982). They appear at the same orbital phases (more rarely as transient phenomena, see Galloway et al. 2016), and they are physically connected with a spectral hardening caused by an increase in soft X-ray absorption (D'Aì et al. 2014). Presence of dips in these disc-fed, short period, systems indicate an inclination angle between $65°$ and $85°$.

In high-mass X-ray systems, dips are more rarely observed, they are not generally periodic, though they are often associated with spectral hardening (see e.g. Naik, Paul & Ali 2011). However, in NGC 247 ULX-1 the lack of any spectral hardening and variation in the absorption column, and the ultrasoft spectrum observed also in the dip phase, suggest that if dips are due to occultation, the covering medium should be extremely opaque (see Section 6.2.1). An alternative scenario involving the presence of a NS and the onset of the propeller effect is discussed in Section 6.2.2.

6.2.1 The occultation scenario

There is a strong hint from all the observations performed until now on this source that dips are not observed when the source is in the SSUL state, but only in the SUL state (see e.g. Feng et al. 2016). If the passage from the SSUL to SUL state is driven by a long-term (of the order of days) variation in the accretion rate, then there must be a feedback mechanism that at the same time alters the properties of the emitting regions and the occulting clouds. In Paper I and Paper II an increase in $\dot{m}$ was invoked to explain both the rise in the observed X-ray luminosity and the appearance of the dips, the latter being produced by higher radiation pressure pushing more optically thick material into our line of sight (see also Gúrpide et al. 2021).

The ionization parameter of the plasma in the wind is defined as $\xi = L_{ion}/(n_H R^2)$, where L_{ion} is the ionizing luminosity, n_H the hydrogen number density, and R the distance from the ionizing source. Assuming the numbers derived in Paper I, we would obtain a wind photosphere $R = 10^{12}$ cm, from which together with the measured $0.17c$ wind velocity provides a traveltime $t = R/v = 200$ s. This is short enough to produce the dips by obscuring the innermost regions. We note that the wind photosphere is comparable to size of the region producing the peaks in the PDS, if we assume Keplerian motion (Alston et al. 2021). A similar value is obtained if we calculate the maximum distance of the wind by assuming that the cloud size does not exceed its distance, i.e. $\Delta R \lesssim R$, and the column density

$N_H \approx n_H C_V \Delta R$ where C_V is the volume filling factor. Assuming a conservative $C_V = 0.1$ and other wind parameters from Paper I, we obtain $R_{max} = L_{ion} C_V / (N_H \xi) \sim 10^{12}$ cm. This is consistent with the wind photosphere predicted for the Galactic super-Eddington accretor SS 433 (see e.g. Fabrika 2004).

Alternatively, following Lamer, Uttley & McHardy (2003), we can rewrite the hydrogen number density as $n_H = N_H / t_{cross} \sqrt{(R/GM)}$, where t_{cross} is the crossing time and M is the mass of the compact object. We find that distances of $\sim 10^{12}$ cm would be associated with a compact object of mass 1–$10\,M_\odot$ and a crossing time between 100 s and a few hours (similar to the dips elapsed times).

We note that some dips are structured, i.e. consisting of multiple events, as suggested by weak re-brightening episodes lasting a few hundreds of seconds. This indicates that the obscuring structure is not uniform but allows a momentary sight of the inner disc.

6.2.2 The propeller scenario

Another possibility to explain dips is the onset of a propeller state. We did not detect any significant coherent signal from our data, which would establish the compact object as an X-ray pulsar. This was, however, expected, given that most of the observed radiation comes from regions distant from the compact object and most of the hard X-ray radiation produced in the inner regions is strongly reprocessed (thus, possibly washing away any coherent signal, especially if short). Assuming the compact object were in any case a strongly magnetized NS, a sufficiently low accretion rate would lead to an increase of the inner disc radius beyond the magnetospheric radius and, as a result, the inner flow would be stopped. We observe dips in SUL2/SUL3 which thus correspond to the lowest accretion rate states. This scenario is consistent with the model by Soria & Kong (2016), which also explains the radius–temperature relation of the BBODY component observed in the normal branch. It also implies that the transition from fainter SSUL to brighter SUL states correspond to epochs in which the wind cone drops owing to a lower accretion rate thereby exposing our line of sight to the bright and hard inner disc regions. The passage from the accretion phase to the 'weak propeller' has a time-scale of around 1 ks. Here we observe that the harder component, which in our interpretation should come from illumination and reprocessing of the internal disc but also from the accretion column, is strongly hampered. Accretion flow, once threaded by the magnetic field lines, can be considered in free-fall, thus turning off very quickly the hard component flux.

The fast variability observed during dips looks remarkably like the one shown by the Hiccup Galactic pulsar, IGR J18245-2452 (see fig. 1 in Ferrigno et al. 2014), although in that case dips were followed by spectral hardening. For NGC 247 ULX-1 two key differences would be at play: super-Eddington accretion and a (likely) high inclination angle (no direct view of the magnetosphere).

Dramatic changes in the observed flux of another pulsating ULX (PULX), M 82 X-2, has also been explained with the propeller scenario (Tsygankov et al. 2016). In that case, the accretor is a 1.37 s accreting pulsar, and the source is observed to switch between two luminosity states at $\sim 1.0 \times 10^{40}$ erg s^{-1} and $\sim 2.8 \times 10^{38}$ erg s^{-1}. Assuming the propeller state sets in when the co-rotation radius ($R_{co} = (GMP^2/4\pi^2)^{1/3}$, where P is the NS spin period) is close to the magnetospheric radius ($R_{mag} = k\dot{M}^{-2/7}\mu^{4/7}(2GM)^{-1/7}$, where k is a geometrical constant factor and μ is the magnetic dipole moment), and the mass accretion rate corresponds to the threshold of the minimum luminosity, an estimate on the pulsar magnetic field

has been derived close to $B \simeq 10^{13}$ G. Similarly, for the PULX NGC 7793 P13 a magnetic field ranging between 1 and 5×10^{12} G was obtained based on the observed spin-up rate and torque model (Fürst et al. 2016; Israel et al. 2017).

In the case of NGC 247 ULX-1 we have no clue on the nature of the compact object, as no flux pulsation has ever been detected. To estimate a possible period, we shall make use of the concept of the limiting luminosity (L_{lim}) of a pulsar before entering the propeller stage (Stella, White & Rosner 1986; Campana et al. 2002). Assuming in the following a standard NS of 1.4 $M_\odot$ mass ($M_{1.4}$) and 10^6 cm (R_6) radius, the limiting luminosity is defined as:

$$L_{lim} \approx \frac{GM\dot{M}_{lim}}{R} \approx 3.9 \times 10^{37} \xi^{7/2} B_{12}^2 P^{-7/3} M_{1.4}^{-2/3} R_6^5 \text{ erg s}^{-1}, \quad (1)$$

where ξ is a geometrical factor that corrects for the disc geometry the classical Alfven radius derived under spherical accretion (we will assume $\xi = 0.5$; see Campana et al. 2018); B_{12} is the NS magnetic field in units of 10^{12} G. At the first order, we assume that such luminosity is reached in the SSUL3 state ($L_{max} \sim 2.5 \times 10^{39}$ erg s^{-1}) as this is the HID region where the source more often resided before dipping. To estimate the deep dip flux we extracted EPIC spectra only for the time intervals where the dip reached the lowest count rate (< 0.1 cps). As expected, the spectral shape remained consistent with the D1 spectrum, while the deep dip flux is 20 ± 10 per cent lower than in D1. We thus obtained $L_{dip} \sim 2.3 \times 10^{38}$ erg s^{-1}. In propeller the observed luminosity is decreased by a factor R_{co}/R, which translates into a dependence on the spin period (see Campana et al. 2002):

$$\frac{L_{lim}}{L_{dip}} \approx R_{co}/R_{NS} = \left(\frac{GMP^2}{4\pi^2 R^3}\right)^{1/3} \approx 170\, P^{2/3}. \quad (2)$$

Given our estimate $L_{lim}/L_{dip} \sim 11$, we derive a spin period of ~ 16 ms and $R_{co} = 107$ km. Because the L_{lim} value is likely a lower limit, also the derived spin period and corotation radius values should be considered as lower limits.

L_{dip} is only marginally above the Eddington limit for a 1.4 $M_\odot$ NS. The fraction of luminosity advected above Eddington scales as a logarithmic power of the total luminosity (see equation 6 in Poutanen et al. 2007), thus the residual advected fraction should be less than 10 per cent. The fraction of power dissipated in the disc out of the corotation radius can thus be expected to be radiatively efficient and directly linked to the corotation radius. We also assume that the remaining kinetic power is efficiently dissipated at the disc boundary (this assumption is tacitly accepted in all works using this formula). The energy dissipated during the accretion phase is thought to be released very close to the NS. Although we do not know how a super-Eddington flow is channelled into the polar caps of the NS, we note that this scenario applied to the cases of known PULXs seem to give consistent results (see Tsygankov et al. 2016). To obtain also an estimate on the possible NS magnetic field value, we will now assume that $R_{mag} \sim R_{co}$. At R_{co} and at the limiting luminosity, the magnetospheric radius expression is

$$R_{mag} \approx 750\, \xi\, B_{12}^{4/7} R_6^{10/7} L_{39}^{-2/7} M_{1.4}^{1/7} \text{ km}. \quad (3)$$

Taking $\xi = 0.5$ and $L_{39} = 2.5$, we derive a field B $\approx 2 \times 10^{11}$ G. Interestingly, this rough estimate is close, but below, the R_{sph} estimate derived by (Paper I) of $\sim 70\, R_g$ (~ 140 km for a $M_{1.4}$ NS). Recent works from Takahashi & Ohsuga (2017) and Chashkina, Abolmasov & Poutanen (2017) provide ad-hoc prescriptions for the magnetospheric radius expression in the super-Eddington regime. We confirm that our first-order estimates are not significantly changed by adopting these more refined formulas.

The inferred moderate magnetic field of NGC 247 ULX-1 is within the range of values derived from the whole PULX sample (King & Lasota [2020]). Galactic high-mass X-ray pulsars show B field higher by up to one order of magnitude (but we also know intermediate $B \sim 10^{11}$ G pulsars like GRO J1744-28; D'Aì et al. [2015]), though their long-term accretion rate is significantly lower than in ULXs. It is still debated how such extreme accretion rates could change the strength and topology of NS magnetic fields (Choudhuri & Konar [2002]; Cumming, Arras & Zweibel [2004]; Lovelace, Romanova & Bisnovatyi-Kogan [2005]); in some cases a significant decrease in the B-value was observed even during an outburst in a strongly magnetized pulsar (see e.g. Cusumano et al. [2016]). The inferred low spin period suggests that the NS could have already been significantly spun-up in the past as most PULXs show periods ~ 1 s. This could be possible only if the accretion rate remained continuously super-Eddington for a sufficiently long time. The sizes and energetics of inflating superbubbles found around many known ULXs confirm that high accretion rates have been sustained for long periods (up to 10^{5-6} yr; Pakull, Soria & Motch [2010]; Soria et al. [2021]).

7 CONCLUSIONS

After two decades of study, state transitions in ULXs and the physics of the super-Eddington accretion are still subjects of lively debate. We have undergone a large campaign with *XMM–Newton* to understand the spectral transitions in the changing-look NGC 247 ULX-1, the brightest known ULX to switch between the supersoft and soft ULX states. Here we summarize our main results:

(1) We obtained a complete characterization of the spectral states in NGC 247 ULX-1 resolving the temporal spectral variations of the source into a limited number of spectral states in the HID. In this diagram, the SSUL state covers a compact and well limited region, whereas the SUL state shows a significantly higher spectral variability. The source spends a comparable time in these states.

(2) We interpreted the softer thermal emission as produced from the outflowing photosphere at the R_{sph}, because the radius and temperature of this component anticorrelate; the hard component flux is the main driver of the motion of the source along the HID.

(3) The dips are observed only in the SUL state and, therefore, their presence appears linked to a threshold accretion rate value. As the source passes along the dipping branch all the emission flux components progressively diminish, but the hard component is comparatively more strongly reduced; the rapid flux decrease and line energy shift of the emission lines during dips indicate that they are produced in the inner regions.

(4) Two possible scenarios can explain dips and state transitions:

(i) If the accretion rate increases from SSUL to SUL, then occultation of the emitting regions from a distant structure is the most likely scenario. A change in the accretion rate would indeed modify the R_{sph} position, and the overall geometry under which the source is observed. The time-scale, if the phenomenon is connected with the outflowing wind, is consistent with the observed ingress–egress duration; quasi-periodic features in the power spectrum indicate the occulting radius $\geq 10^4 R_g$.

(ii) If the accretion rate decreases from SSUL to SUL, then we proposed the onset of a propeller state. The lower accretion rate in the upper SUL state is mostly supported by the $R_{bb} - T_{bb}$ anticorrelation of the softer component, which is in agreement with expanding photosphere model of Soria & Kong ([2016]). Assuming $R_{mag} \sim R_{co}$, we estimated a relatively low spin period of 16 ms and a NS magnetic field $\approx 2 \times 10^{11}$ G.

DATA AVAILABILITY

All the data used in this article are publicly available from ESA *XMM–Newton* Science Archive (XSA; https://www.cosmos.esa.int/web/xmm-newton/xsa) and NASA HEASARC archive (https://heasarc.gsfc.nasa.gov/). Light curves and spectra are available from the author upon request.

REFERENCES

Alston W. N. et al., 2021, MNRAS, 505, 3722 (Paper II)
Ambrosi E., Zampieri L., 2018, MNRAS, 480, 4918
Bachetti M. et al., 2014, Nature, 514, 202
Barret D., Decourchelle A., Fabian A., Guainazzi M., Nandra K., Smith R., den Herder J.-W., 2020, Astron. Nachr., 341, 224
Campana S., Stella L., Israel G. L., Moretti A., Parmar A. N., Orlandini M., 2002, ApJ, 580, 389
Campana S., Stella L., Mereghetti S., de Martino D., 2018, A&A, 610, A46
Chashkina A., Abolmasov P., Poutanen J., 2017, MNRAS, 470, 2799
Choudhuri A. R., Konar S., 2002, MNRAS, 332, 933
Cumming A., Arras P., Zweibel E., 2004, ApJ, 609, 999
Cusumano G., La Parola V., D'Aì A., Segreto A., Tagliaferri G., Barthelmy S. D., Gehrels N., 2016, MNRAS, 460, L99
D'Aì A., Iaria R., Di Salvo T., Riggio A., Burderi L., Robba N. R., 2014, A&A, 564, A62
D'Aì A. et al., 2015, MNRAS, 449, 4288
Davidge T. J., 2006, ApJ, 641, 822
Fabrika S., 2004, ASPR, 12, 1
Feng H., Tao L., Kaaret P., Grisé F., 2016, ApJ, 831, 117
Ferrigno C. et al., 2014, A&A, 567, A77
Fürst F. et al., 2016, ApJ, 831, L14
Galloway D. K., Ajamyan A. N., Upjohn J., Stuart M., 2016, MNRAS, 461, 3847
Gieren W. et al., 2009, ApJ, 700, 1141
Grisé F., Kaaret P., Corbel S., Feng H., Cseh D., Tao L., 2012, ApJ, 745, 123
Grisé F., Kaaret P., Corbel S., Cseh D., Feng H., 2013, MNRAS, 433, 1023
Gu W.-M., Sun M.-Y., Lu Y.-J., Yuan F., Liu J.-F., 2016, ApJ, 818, L4
Guo J., Sun M., Gu W.-M., Yi T., 2019, MNRAS, 485, 2558
Gúrpide A., Godet O., Vasilopoulos G., Webb N. A., Olive J. F., 2021, preprint (arXiv:2106.05708)
Israel G. L., Stella L., 1996, ApJ, 468, 369
Israel G. L., Esposito P., Rodríguez Castillo G. A., Sidoli L., 2016, MNRAS, 462, 4371
Israel G. L. et al., 2017, MNRAS, 466, L48
Jin J., Feng H., Kaaret P., Zhang S.-N., 2011, ApJ, 737, 87
Kaaret P., Feng H., Roberts T. P., 2017, ARA&A, 55, 303
King A., Lasota J.-P., 2020, MNRAS, 494, 3611
Kosec P. et al., 2018, MNRAS, 479, 3978
Lamer G., Uttley P., McHardy I. M., 2003, MNRAS, 342, L41
Lovelace R. V. E., Romanova M. M., Bisnovatyi-Kogan G. S., 2005, ApJ, 625, 957
Meier D. L., 2012, Black Hole Astrophysics: The Engine Paradigm. Springer, Berlin
Middleton M. J., Walton D. J., Roberts T. P., Heil L., 2014, MNRAS, 438, L51

Middleton M. J., Heil L., Pintore F., Walton D. J., Roberts T. P., 2015, MNRAS, 447, 3243

Mushtukov A. A., Portegies Zwart S., Tsygankov S. S., Nagirner D. I., Poutanen J., 2021, MNRAS, 501, 2424

Naik S., Paul B., Ali Z., 2011, ApJ, 737, 79

Pakull M. W., Soria R., Motch C., 2010, Nature, 466, 209

Pinto C., Middleton M. J., Fabian A. C., 2016, Nature, 533, 64

Pinto C. et al., 2017, MNRAS, 468, 2865

Pinto C. et al., 2021, MNRAS, 505, 5058 (Paper I)

Pintore F., Esposito P., Zampieri L., Motta S., Wolter A., 2015, MNRAS, 448, 1153

Poutanen J., Lipunova G., Fabrika S., Butkevich A. G., Abolmasov P., 2007, MNRAS, 377, 1187

Robba A. et al., 2021, A&A 652 A118

Rodríguez Castillo G. A. et al., 2020, ApJ, 895, 60

Shakura N. I., Sunyaev R. A., 1973, A&A, 500, 33

Shen R. F., Barniol Duran R., Nakar E., Piran T., 2015, MNRAS, 447, L60

Soria R., Kong A., 2016, MNRAS, 456, 1837

Soria R., Pakull M. W., Motch C., Miller-Jones J. C. A., Schwope A. D., Urquhart R. T., Ryan M. S., 2021, MNRAS, 501, 1644

Stella L., White N. E., Rosner R., 1986, ApJ, 308, 669

Stobbart A. M., Roberts T. P., Warwick R. S., 2004, MNRAS, 351, 1063

Sutton A. D., Roberts T. P., Middleton M. J., 2015, ApJ, 814, 73

Takahashi H. R., Ohsuga K., 2017, ApJ, 845, L9

Takeuchi S., Ohsuga K., Mineshige S., 2013, PASJ, 65, 88

Tao L., Feng H., Kaaret P., Grisé F., Jin J., 2012, ApJ, 758, 85

Tsygankov S. S., Mushtukov A. A., Suleimanov V. F., Poutanen J., 2016, MNRAS, 457, 1101

Urquhart R., Soria R., 2016, MNRAS, 456, 1859

Verner D. A., Ferland G. J., Korista K. T., Yakovlev D. G., 1996, ApJ, 465, 487

Walton D. J., et al., 2018, ApJ, 856, 128

Walton D. J. et al., 2020, MNRAS, 494, 6012

White N. E., Swank J. H., 1982, ApJ, 253, L61

Wilms J., Allen A., McCray R., 2000, ApJ, 542, 914

XRISM Science Team, 2020, preprint (arXiv:2003.04962)

Yao Y., Feng H., 2019, ApJ, 884, L3

This paper has been typeset from a TEX/LATEX file prepared by the author.